Effect of sample preparation techniques upon single cell chemical imaging: A practical comparison between synchrotron radiation based X-ray fluorescence (SR-XRF) and Nanoscopic Secondary Ion Mass Spectrometry (nano-SIMS)

Björn De Samber [a, b, *], Riet De Rycke [c, d], Michiel De Bruyne [c, d], Michiel Kienhuis [e], Linda Sandblad [f], Sylvain Bohic [g, h], Peter Cloetens [h], Constantin Urban [i], Lubos Polerecky [e], Laszlo Vincze [a]

[a] Department of Chemistry, Ghent University, Ghent, Belgium
[b] Imec — Vision Lab, University of Antwerp, Wilrijk, Belgium
[c] Department for Biomedical Molecular Biology, Ghent University, Belgium and VIB Center for Inflammation Research, Ghent, Belgium
[d] Ghent University Expertise Centre for Transmission Electron Microscopy and VIB Bio-Imaging Core, Ghent, Belgium
[e] Department of Earth Sciences — Geochemistry, Faculty of Geosciences, Utrecht University, the Netherlands
[f] Department of Molecular Biology, Umeå University, Umeå, Sweden
[g] Inserm, UA07, Synchrotron Research for Biomedicine, Grenoble, France
[h] European Synchrotron Radiation Facility, Grenoble, France
[i] Department of Clinical Microbiology, Umeå University, Umeå, Sweden

HIGHLIGHTS

- First Nano-SIMS imaging of thin sections of human polymorphonuclear neutrophils (PMNs) embedded in Spurr's resin.
- Nano-SIMS and SR nano-XRF techniques are compared for nanochemical imaging of PMNs embedded in Spurr's resin.
- Trace level metal imaging at 50 nm spatial resolution of cryofrozen PMNs using SR nano-XRF.
- Comparison of SR nano-XRF imaging on 1) thin sections of PMNs embedded in Spurr's resin and 2) whole, cryofrozen PMNs.

GRAPHICAL ABSTRACT
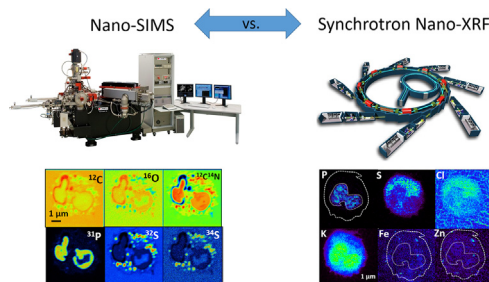
ARTICLE INFO

ABSTRACT

Analytical capabilities of Nanoscopic Secondary Ion Mass Spectrometry (nano-SIMS) and Synchrotron Radiation based X-ray Fluorescence (SR nano-XRF) techniques were compared for nanochemical imaging of polymorphonuclear human neutrophils (PMNs). PMNs were high pressure frozen (HPF), cryo-substituted, embedded in Spurr's resin and cut in thin sections (500 nm and 2 μm for both techniques resp.) Nano-SIMS enabled nanoscale mapping of isotopes of C, N, O, P and S, while SR based nano-XRF enabled trace level imaging of metals like Ca, Mn, Fe, Ni, Cu and Zn at a resolution of approx. 50 nm. The obtained elemental distributions were compared with those of whole, cryofrozen PMNs measured at

* Corresponding author. imec - Vision Lab, Dept. Physics, University of Antwerp
Universiteitsplein 1, Building, N B-2610, Antwerp.
E-mail address: Bjorn.DeSamber@UAntwerpen.be (B. De Samber).

the newly developed ID16A nano-imaging beamline at the European Synchrotron Radiation Facility (ESRF) in Grenoble, France. Similarities were observed for elements more tightly bound to the cell structure such as phosphorus and sulphur, while differences for mobile ions such as chlorine and potassium were more pronounced. Due to the observed elemental redistribution of mobile ions such as potassium and chlorine, elemental analysis of high pressure frozen (HPF), cryo-substituted and imbedded cells should be interpreted critically. Although decreasing analytical sensitivity occurs due to the presence of ice, analysis of cryofrozen cells - close to their native state - remains the golden standard. In general, we found nanoscale secondary ion mass spectrometry (nano-SIMS) and synchrotron radiation based nanoscopic X-ray fluorescence (SR nano-XRF) to be two supplementary alternatives for nanochemical imaging of single cells at the nanoscale.

1. Introduction

Among the label-free, elemental imaging techniques (i.e. no chemical staining, no fluorescent probes), capable of subcellular resolution, two techniques especially stand out: synchrotron radiation-based nanoscopic X-ray fluorescence (SR nano-XRF) and nanoscale secondary ion mass spectrometry (nano-SIMS). Both nano-SIMS [1–6] and SR nano-XRF [7–14] have already been used extensively for nano-imaging of cells and tissues. Although both techniques provide nanochemical imaging, they differ in a number of aspects. While nano-SIMS bombards the sample surface with a focused ion beam, resulting in sputtered secondary ions, nano-XRF ejects inner core-shell electrons, resulting in secondary fluorescent photons. The main analytical difference is that nano-SIMS can distinguish between different isotopes of the same element (e.g., ^{56}Fe and ^{57}Fe), whereas SR nano-XRF imaging only relates to the atomic number. Table 1 provides an overview of the most important properties and differences of both techniques with emphasis on cell imaging. In principle, both techniques are available for the general scientific community upon request, taking into account their availability.

Both nano-SIMS and SR based nano-XRF significantly differ in terms of required sample preparation. For nano-SIMS, samples need to be made compatible with a high vacuum environment and need to be made as flat as possible, ideally few nanometers. Biological samples for nano-SIMS analysis are therefore first chemically (or cryogenically) fixed. To establish cryogenic fixation, high pressure freezing (HPF) is the best method as it avoids damage of the cell ultrastructure which would otherwise take place during slow freezing, generating ice crystals [15–18]. Although the required following cryo-substitution step can slow down the diffusion of unbound elements such as potassium, the complete retention of other elemental distributions with this method is unlikely. Following cryo-substitution, samples are embedded in a resin (e.g. Spurr, LR white), cut in (sub)micrometer thin-sections, deposited onto pure conducting silicon chips (or polycarbonate filter paper) and, when necessary, gold-coated to avoid charging. Although not yet commercially available, work is ongoing to develop analysis of cryogenically frozen specimens with nano-SIMS (5). With respect to sample preparation for SR-XRF scanning of biological samples, majority of samples is still analyzed under ambient temperature and atmosphere. In this case, the stability of

Table 1
Comparison of nano-SIMS and SR nano-XRF analytical techniques.

Property	Analytical technique	
	Nano-SIMS	SR nano-XRF
probe	focused ion beam (Cs^+ or O^-)	focused high-energy photon beam
energy	16 keV (both Cs^+ and O^-)	~8-20 keV (this experiment: 17.1 keV)
analytical signal	mass-to-charge ratio of sputtered ions	X-ray fluorescent photons (XRF)
measurement condition	high vacuum	air or vacuum (+cryo)
imaging manner	sample position is fixed, ion beam is deflected	X-ray beam is fixed, sample is scanned through X-ray beam
rastering condition	multiple planes, ~1 ms dwell time	one plane, ms−s dwell time
probed depth	few atomic layers	element dependent (μm to mm)
destructiveness of method	atoms are physically ejected	possible radiation damage
multi-element character	up to 7 either positive OR negative ions	yes, if no spectral overlap
element range	from H to U	from Na to U
spatial resolution	• Cs^+ source (non-metals): 50 nm • O^- duoplasmatron (metals): 200 nm • RF source (new prototype): 50 nm • sample/element dependent!	• down to 30 nm • sample-independent
isotopic resolution	Yes	No
sample preparation (for cells)	• Cryofixation, cryosubstitution/embedding + thin sectioning • conducting and flat sample required (e.g. via gold coating)	• also cryofrozen samples possible • no requirement for flat sample!
usual support (for cells)	silicon wafer, polycarbonate filter	silicon nitride membrane
calibration work instrument	source choice, beam alignment, mass selection + optimization	beam alignment, detector optimization
element maps	instantaneous	spectral fitting
availability	• lab instrument, mainly in university context • to be discussed with nano-SIMS facility	• international facility • application form + review process • large oversubscription factor!
cost	generally few k€ for several days of analysis (often based on cost of service contract)	for universities: • travel/lodging costs reimbursed • no analysis cost

the sample throughout the X-ray scanning procedure is assured by chemical fixation followed by embedding, or cryofixation followed by freeze-drying. As sample support for cells, silicon nitride (Si_3N_4) membranes are often the preferred choice, resulting in minimal X-ray scatter and low XRF background.

Recently, few hard X-ray nanoprobes worldwide are offering chemical analysis under cryogenic conditions: cryofrozen (vitrified) samples can be directly inserted in the instrument without the need of chemical fixation and embedding or freeze-drying [9,19]. Prior chemical sample preparation merely involves a few second wash of the silicon nitride wafers with adhered cells with a metal-free buffer solution (e.g. ammonium acetate), removing unwanted trace metals from the original medium. The procedure is followed by gentle blotting of the wafer to remove the excess layer of water covering the cells, causing detrimental absorption of fluorescent X-rays when frozen. Then, intra- and extracellular content are vitrified via manual (or automated) plunge freezing in a cryogen (typically isopentane cooled at −150 °C). Note that since plunge freezing is not effected under high pressure as is the case for HPF, it may result in unwanted artefacts such as ice layers, cracks, ice crystals. Nevertheless plunge freezing is required for larger samples as they are not compatible with HPF instruments. Vitrified samples are then further cooled in liquid nitrogen, transported to the synchrotron in a dry-shipper and finally inserted into the cryogenic sample environment of the beamline, maintaining the samples at cryogenic temperature uninterruptedly and ensuring the cryogenic workflow.

In this manuscript, the analytical capabilities of nano-SIMS and SR nano-XRF are compared for chemical imaging of single cells, and the effect of required sample preparation methods upon the elemental distribution is critically investigated. For practical reasons, the comparison between the different techniques is illustrated on one specific cell type, i.e. polymorphonuclear neutrophils (or PMNs), which are circulating short-lived cells of the innate immune system with a large antimicrobial arsenal and serve as a first line of defense against pathogens [20,21]. One of these defense mechanisms is the formation of neutrophil extracellular traps (or NETs), in which pathogens get ensnared and killed [22–26]. For metal imaging of PMNs using nano-SIMS, a conventional oxygen duoplasmatron source was deployed. Although such source is advised for imaging of metal ions, it achieves lower resolution (min. 200 nm) compared to a cesium source (50 nm) used for imaging of non-metals. Recently, a radiofrequency (RF) oxygen plasma source has become commercially available reaching approx. 40 nm resolution and 5-45 times higher sensitivity for electropositive elements [28]. However, due to its high cost and low available, such source was not used in this study. All synchrotron nano-XRF experiments were performed at the European Synchrotron Radiation Facility (ESRF): initially at the ID22NI beamline, followed by its successor, the ID16A 'Nano-Imaging' beamline, currently providing the world's brightest X-ray nanobeam (flux 10^{11} photons/s and 50 nm beam size) and additionally equipped with a state-of-the-art cryogenic sample environment, maintaining cryofrozen samples at approx. 150 K [27]. First, we compare elemental distributions in thin sections of PMNs embedded in Spurr's resin obtained through nano-SIMS and nano-XRF measurements under ambient temperature. Second, these results are compared with SR nano-XRF scanning of whole, cryogenically frozen PMNs measured at the ESRF's ID16A beamline. In this way, we hope to provide the biologist with more insight whether nano-SIMS or nano-XRF should be used for his/her elemental imaging research in cells. Additionally, we hope to lift a tip of the veil about the effect of sample preparation techniques associated with these techniques on the element distributions obtained.

2. Results and discussion

2.1. Nano-SIMS imaging of high pressure frozen, cryosubstituted human neutrophils (PMNs)

Fig. 1a shows a light microscopy image of the 500 nm thin slabs of embedded PMNs deposited on a silicon chip of 5×5 mm^2. To enable the analysis, PMNs were first vitrified using high pressure freezing (HPF), followed by cryo-substitution in Spurr's resin which is, from the chemical/elemental point of view, a mixture of organics containing only hydrogen, carbon, oxygen and nitrogen [28]. Afterwards, the resin samples were thin-sectioned using a microtome (see Materials and Methods section for more information). From the Spurr's resin cube, 70 nm thin sections were cut for transmission electron microscopy (TEM) imaging, while 500 nm thin sections were cut for nano-SIMS. Fig. 1a shows a visible light microscope image of a 500 nm thin quasi-circular section (deposited on silicon) containing hundreds of neutrophils visible as small, pink dots. Fig. 1b shows a TEM image of a single, randomly chosen PMN located within a 70 nm section, cut adjacent to the 500 nm thin section used for nano-SIMS analysis. The two darker regions are part of the PMN's lobulated nucleus, while white area between nucleus and cytoplasm has likely been caused by artefacts from the HPF and/or chemical fixation: the denser the structure (the nucleus in this case), the less water it contains and the better the cryofixation (due to less formation of ice crystals). On the other hand, denser structures sometimes require more time to allow the resin to penetrate the tissue. However, for this specific case, no ice crystals are visible and the artefact is likely caused by osmotic pressure differences between nucleus and cytoplasm. The latter can be solved by changing infiltration times and/or an adapted cryoprotectant [29].

The white rectangle in Fig. 1a indicates the PMN which was imaged by nano-SIMS. Nano-SIMS imaging was performed at Utrecht University using the NanoSIMS 50 L instrument from Cameca, equipped with a cesium and oxygen duoplasmatron source. Pure silicon wafers were used as substrate for measuring 500 nm thin sample sections since they avoid charging, are readily available, strong and cheap. In general, we observed better quality of nano-SIMS images after the thin sections were pre-sputtered with the cesium source. This process implants cesium atoms into the sample, which leads to higher secondary ion yields and thus better signal-to-noise ratio. Fig. 1c shows isotopic maps of ^{12}C, ^{16}O, ^{12}C^{14}N, ^{31}P, ^{32}S and ^{34}S of the PMN indicated with a white rectangle in Fig. 1a, and measured using the cesium(Cs)-source. Note that when using the nano-SIMS Cs-source, elements such as C, O and N can be imaged, privileging this source to investigate lighter elements in single cells. The basic morphology of the PMN is clearly recognizable in the maps of ^{12}C, ^{16}O and ^{12}C^{14}N. Although the size of a single pixel in the isotope maps is 20 nm, the actual resolution was estimated at approx. 200 nm/pixel (more accurate estimations of the resolution were not performed as this was considered beyond the available time and scope of this study). Note also that spatial resolution achievable with nano-SIMS is sample-dependent; better conducting samples typically provide higher imaging resolution. Interestingly, regions containing the highest ^{12}C^{14}N ion counts also appear darkest in the TEM image in Fig. 1b, indicating their lower electron density. Due to the presence of phosphorus-containing DNA in the lobulated nucleus of the PMNs, ^{31}P is strongly present. Smaller granules in the cytoplasm are rich in ^{32}S, ^{34}S and ^{12}C^{14}N, indicating their sulphur- and nitrogen-rich protein content; the presence of sulphur-rich proteins within antimicrobial granules has indeed been reported for PMNs [30,31]. More phosphorous is present on the outer, i.e. perinuclear region of the nucleus, characterized at the same time by less sulphur present.
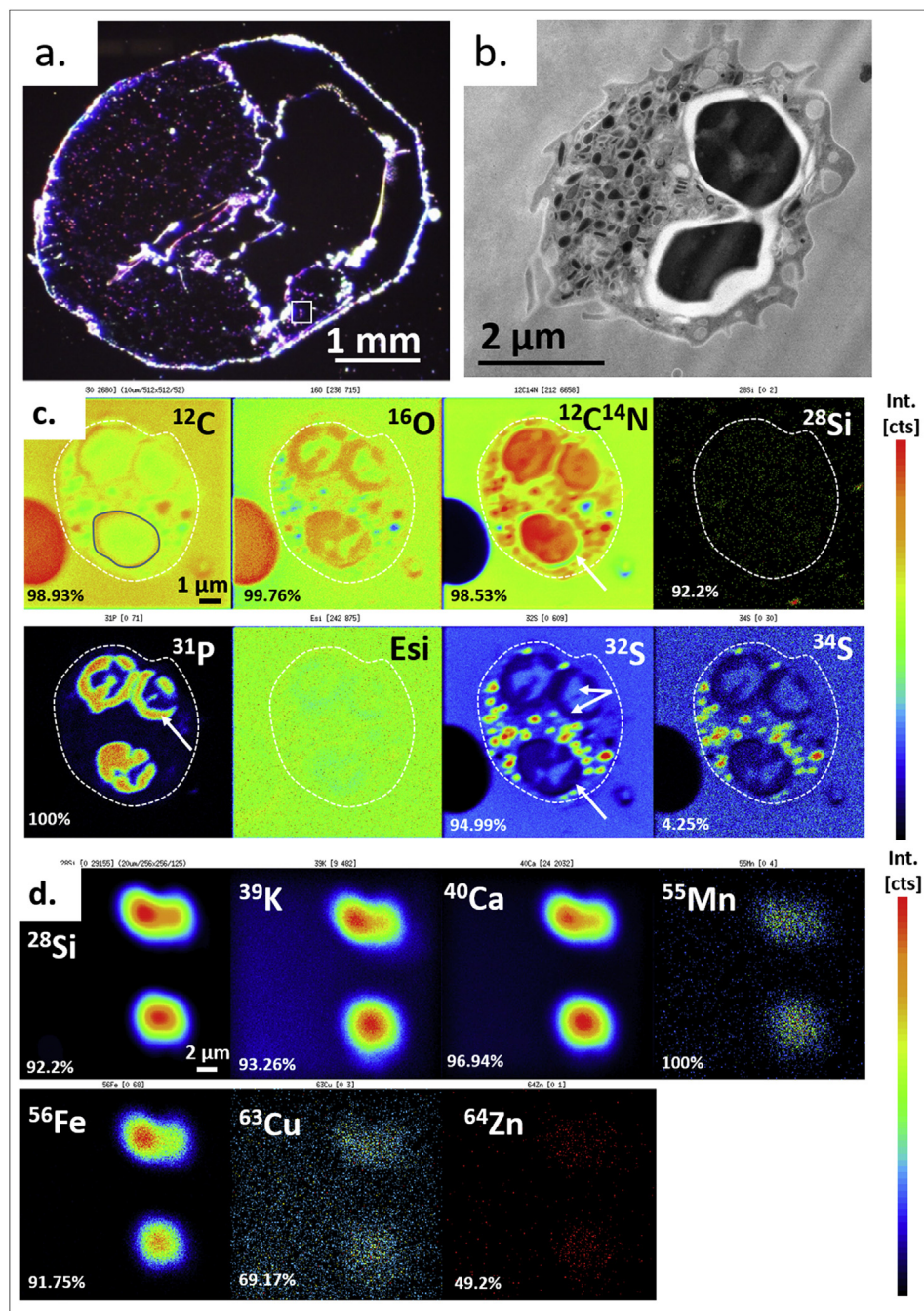
Fig. 1. a) microscope image of a 500 nm thin section of Spurr's resin, containing hundreds of single PMNs from control culture. Region indicated with a white rectangle indicates the PMN scanned with nano-SIMS. b) TEM image of a single PMN from the same control culture c) distribution of ^{12}C, ^{16}O, ^{12}C^{14}N, ^{28}Si, ^{31}P, Esi (electron secondary ionization), ^{32}S, ^{34}S in a single PMN from control culture (cesium source, 10×10 μm^2, 512×512 pixels, 20 nm/pixel, 100 planes, 2 pA, pre-sputtered for 15 min with 10 pA), the cell membrane of the PMN is indicated with a white dashed line, d) distribution of ^{28}Si, ^{39}K, ^{40}Ca, ^{56}Fe, ^{55}Mn, ^{63}Cu, ^{64}Zn (oxygen duoplasmatron source, 200 pA, 20×20 μm^2, 256×256 pixels, 80 nm/pixel, 157 planes, no pre-sputtering). In c) and d), natural abundance of the measured isotope is given in the lower left corner of each map. Color bar on the right hand side represents secondary ion counts; min. and max. intensity value is provided above each isotope map (between square brackets). (For interpretation of the references to colour in this figure legend, the reader is referred to the Web version of this article.)

A ^{12}C^{14}N- and ^{32}S-poor and ^{12}C-rich region is also present between nucleus and cytoplasm (indicated with a white arrow in Fig. 1c), which we believe to be an result from the Spurr's resin infiltration.

Imaging of metals requires bombardment of the sample surface with negative ions. Therefore, the cesium source was exchanged to the available oxygen duoplasmatron source and the instrument was tuned to allow the detection of biologically relevant metals ^{39}K, ^{40}Ca, ^{55}Mn, ^{56}Fe, ^{63}Cu and ^{64}Zn. Since the supporting wafer was

made from pure silicon, the ^{28}Si isotope was monitored as well. A PMN from control culture was scanned, located on the same thin section as the PMN shown in Fig. 1a. The metal imaging results with the nano-SIMS duoplasmatron source are shown in Fig. 1d. To image two possible PMN candidate cells simultaneously, the field of view was taken twice as large compared to Fig. 1c (20×20 μm^2 instead of 10×10 μm^2). Unfortunately, a significantly lower spatial resolution is obtained when deploying the oxygen source (Fig. 1d)

compared to the cesium source (Fig. 1c). In Fig. 1d, isotope maps of ^{28}Si, ^{39}K, ^{40}Ca, ^{56}Fe, ^{55}Mn, ^{56}Fe and ^{63}Cu all show two spherical structures which, given their size, likely represent entire PMNs. Although the ^{56}Fe isotopic map (trace level amounts) still provides an acceptable signal-to-noise ratio, ^{55}Mn, ^{63}Cu and ^{64}Zn are close to the limit of detection (LOD). For obtaining depth-resolved information, hundred planes were measured overnight, which did not yield significantly different info. As already mentioned in the introduction, an RF oxygen plasma source has been recently developed reaching approx. 40 nm resolution and 5-45 times higher sensitivity for electropositive elements which would provide superior metal imaging capability compared to the oxygen duoplasmatron source used in our case [32]. Due to the limited availability of this source and its high cost, this option was not explored within this work.

Fig. 2 shows TEM and nano-SIMS imaging of control culture PMNs and PMNs releasing so-called neutrophil extracellular traps (NETs). NETs are recently discovered fibrous structures in which pathogens get ensnared and killed [22–26]. NETs are of interest for elemental imaging as they potentially contain proteins harvesting essential metals from pathogens [25,33–35]. Under *in vitro* conditions, NET-formation can be induced using PMA (phorbol myristate acetate). In our study, PMN cell cultures were exposed to PMA for 1 h and 2 h and then high pressure frozen at specific time intervals (in a reverse-time course series). Due to the lower resolution and sensitivity of the oxygen duoplasmatron source, stimulated PMNs were investigated with nano-SIMS using the cesium source only. Electron multiplier detectors of the nano-SIMS were optimized for the following isotopes: ^{12}C, ^{16}O, $^{12}C^{14}N$, ^{31}P, ^{31}S and ^{32}S. Note that in Fig. 1c, nano-SIMS isotope maps of a single PMN from control culture are already provided once; Fig. 2a shows measurements of another PMN from the same control culture. As in Fig. 1c, Fig. 2a shows strong presence of phosphorus in the perinuclear region and presence of sulphur as granules within the cytoplasm. A $^{12}C^{14}N$, ^{31}P, and ^{32}S-poor and ^{12}C, ^{16}O-rich region is also present between nucleus and cytoplasm, which we hypothesize to be a sample
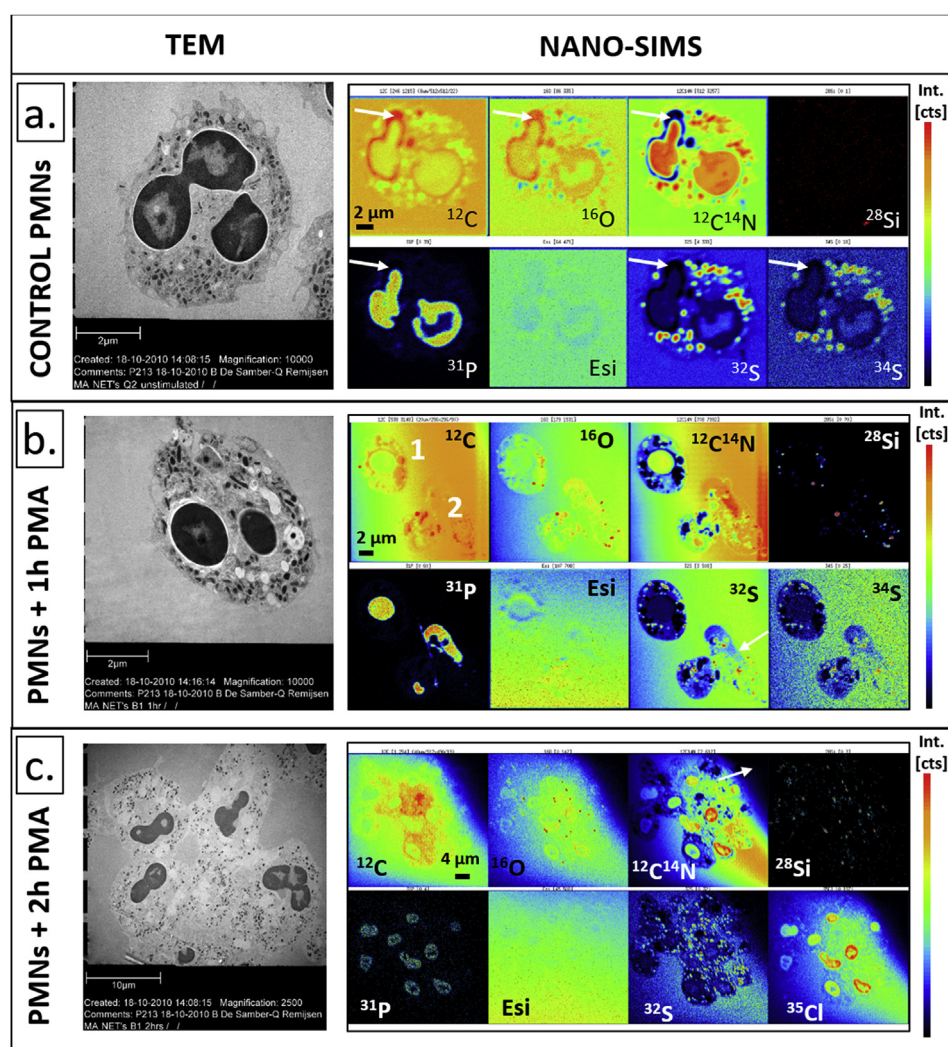

Fig. 2. a) Nano-SIMS and TEM images of PMNs from control culture (upper row), b) PMNs exposed to PMA for 1 h (middle row), c) PMNs exposed to PMA for 2 h (lower row). Isotopic maps are shown for: ^{12}C, ^{16}O, $^{12}C^{14}N$, ^{31}P, ^{32}S and ^{34}S (^{34}S replaced by ^{35}Cl for 2 h PMA stimulation case). Spurr's resin thin section used for TEM (70 nm thickness) and for nano-SIMS (500 nm thickness) originate from the same resin cube. Image parameters for the nano-SIMS measurements are: 16×16 μm^2 area, 1024×1024 pixels, 16 nm/pixel, 100 planes (control PMNs), 20×20 μm^2 area, 256×256 pixels, 80 nm/pixel, 50 planes (1 h PMA exposure), 40×40 μm^2 area, 512×512 pixels, 80 nm/pixel, 19 planes (2 h PMA exposure). Color bar on the right hand side represents secondary ion counts; min. and max. intensity value is provided above each isotope map (between square brackets). (For interpretation of the references to colour in this figure legend, the reader is referred to the Web version of this article.)

preparation artefact caused by differential migration of the resin into the cell (see previous paragraph). Although not performed upon the same cell, PMN morphology obtained via TEM images can be clearly correlated to the nano-SIMS isotopic maps: after 1 h PMA stimulation (Fig. 2b), PMN no. 1 (upper left) remains intact, while PMN no. 2 (lower right) seems to have burst open. Although this could represent cell damage that occurred during sample preparation, it may also represent release of the PMNs intracellular content to the extracellular environment, indicating NET formation. Note that due to the limited number of measuring days on the SIMS instrument available and our aim to image several PMNs together, the field of view differs across the different PMA exposure times. In Fig. 2c, the TEM image of PMNs stimulated with PMA for 2 h (40×40 μm^2) shows significant increase of the surface area of all PMNs. Also, the PMN nuclei reside in one common cytoplasmic 'pool'. This morphological change can also be clearly recognized in the nano-SIMS isotopic map of ^{12}C, ^{16}O, $^{12}C^{14}N$, ^{31}P and ^{32}S. Note that for the 2 h PMA stimulation case - measured at a later stage - also ^{35}Cl isotope was optimized and measured. Therefore, the ^{34}S map has been replaced in Fig. 2c with ^{35}Cl isotope, which is predominantly present in the PMN nuclei. For an unknown reason, the ^{16}O and ^{28}Si isotope map reveal hot-spots in PMA-stimulated PMNs, which are not present in the PMNs from control culture. Although during PMA stimulation reactive oxygen species (or ROS) are formed by PMNs to create a hostile environment for the pathogen [30,36], the reason for increased presence of ^{16}O and ^{28}Si in Fig. 2b–c is unknown (isobaric interference is very unlikely since the mass resolving power reached 11,000). Note that the background in Fig. 2c is not uniform due to implantation and/or charging effects. In general, throughout 1-2 h PMA stimulation, nano-SIMS elemental maps could be clearly correlated with TEM imaging obtained from the same sample cube (Spurr's resin). Due to the lower imaging resolution of the oxygen duoplasmatron source available, metal imaging was not further pursued.

2.2. Comparison of nano-SIMS and SR nano-XRF imaging upon high pressure frozen and cryosubstituted PMNs

In this section, we compare chemical imaging of thin-sections (Spurr's resin) of single PMNs using 1) nano-SIMS equipped with cesium-source and 2) synchrotron nano-XRF performed under ambient temperature and pressure [26,37]. SR nano-XRF experiments under ambient temperature and pressure were performed at the former ID22NI 'nano-imaging beamline' at the European Synchrotron Radiation Facility (ESRF) in Grenoble, France [38]. Sections were cut from the same resin cubes as for the nano-SIMS analysis shown in Fig. 1. Since XRF is a deeply penetrating technique compared to surface-sensitive nano-SIMS (cf. Table 1), sections for nano-XRF were cut thicker (2 μm instead of 500 nm), which increases the amount of probed mass and therefore the signal. Sections were deposited on 500 nm thin silicon nitride (Si_3N_4) membranes instead of silicon wafers, which are free of trace metals and generate minimal background. The upper and middle panel of Fig. 3 show the comparison of nano-SIMS (a) and SR based nano-XRF imaging (b) on Spurr's resin thin section of a single PMN from control culture (high pressure frozen and cryo-substituted before). Pixel size of nano-SIMS maps are estimated to be 16 nm/pixel, although true spatial resolution is approx. 100-200 nm. Pixel size of nano-XRF elemental maps is 50 nm, which is close to the experimentally determined X-ray beam size and dwell time per pixel is 300 ms. Nano-SIMS maps (Fig. 3a) provide information on the elements carbon, oxygen and nitrogen, which cannot be probed with XRF. Light elements like P, S and Cl can however be probed via nano-XRF (see Fig. 3b). In Fig. 3b, SR nano-XRF elemental maps are presented in counts (300 ms dwell time/pixel). Note that

quantification of nano-SIMS elemental maps is still considered difficult to put into practice due to matrix differences between standard and sample.

In Fig. 3a (nano-SIMS), we observe a higher sensitivity for the elements phosphorus and sulphur compared to Fig. 3b (nano-XRF), which is likely due to the absorption of fluorescence within the Spurr's resin and the succeeding air path when using nano-XRF (see Fig. 3b). Measuring the sections using SR nano-XRF under vacuum conditions would improve this issue, but was not available for this particular beamline (ID22NI). Note that for lower atomic number elements such as P and S, elemental maps obtained by nano-XRF only have few μm probing depth and are in essence more representative for the surface of the sample, and therefore likely more similar (but not necessarily identical) to nano-SIMS isotopic maps. Interestingly, in Fig. 3b (SR nano-XRF, ambient temperature and pressure), sulphur is not visible anymore in the PMN cytoplasm, which can only be caused by lower sensitivity (see earlier) or an effect of the sample preparation. In Fig. 3b, element distributions for trace metals K, Ca, Mn, Fe, Co, Ni, Cu and Zn with 50 nm spatial resolution are provided, which was not achievable with nano-SIMS oxygen duoplasmatron source. This stresses the unique capability of SR nano-XRF for trace level imaging in single cells (not considering the capabilities of a nano-SIMS RF oxygen source, which was not used in this work). Also note that a larger number of elements - only limited by spectral overlap - is probed with nano-XRF, compared to a fixed number of seven isotopes with nano-SIMS. Even higher atomic number elemental maps of biologically relevant non-metals can be probed, such as bromine and iodine. Although this paragraph provides a clear comparison between analytical capabilities of nano-SIMS and SR based nano-XRF for elemental imaging of single cells embedded in Spurr's resin, question remains whether metal distributions are preserved using this sample preparation method. This issue will be addressed in the next section.

2.3. Comparison of nano-SIMS imaging on cryosubstituted thin sections with SR based nano-XRF on entire, cryofrozen PMNs

To verify to which extent the elemental distributions of PMNs obtained from thin sections (Spurr's resin) are corresponding to those of native PMNs, additional measurements were performed at the newly available ID16NI 'nano-imaging' beamline. ID16NI beamline is equipped with a high vacuum, cryogenic sample environment and an entire cryogenic workflow to insert vitrified samples [9,27]. Fig. 3c shows SR nano-XRF measurements of a single, cryofrozen PMN (dwell time 300 ms, 50 nm pixel size). In contrast to the nano-XRF measurements under ambient temperature/pressure of PMN thin sections shown in Fig. 3b, *entire* PMNs are measured under cryogenic condition since production of micrometer-thick vitrified cryosections remains a challenge [39]. Quantification of element maps obtained via nano-XRF was performed via measuring a standard under identical conditions (AXO Thin Film or NIST SRM 1577C 'bovine liver') and by the Fundamental Parameter (FP) quantification method, including self-absorption correction for the SRM and for the ice layer covering the sample, and background. For more information concerning the XRF quantification method applied, we refer to earlier work [9].

Interestingly, element distributions of phosphorus and sulphur in Fig. 3c have a higher agreement with the nano-SIMS measurements on cryo-substituted thin sections (see Fig. 3a) than with the nano-XRF measurements under ambient temperature (Fig. 3b). This likely indicates the (partial) preservation of phosphorous and sulphur for the cryo-substitution technique. In Fig. 3c, chlorine is clearly more concentrated in the cytoplasm for the cryofrozen PMN, compared to the cryo-substitution case (Fig. 3b), suggesting a
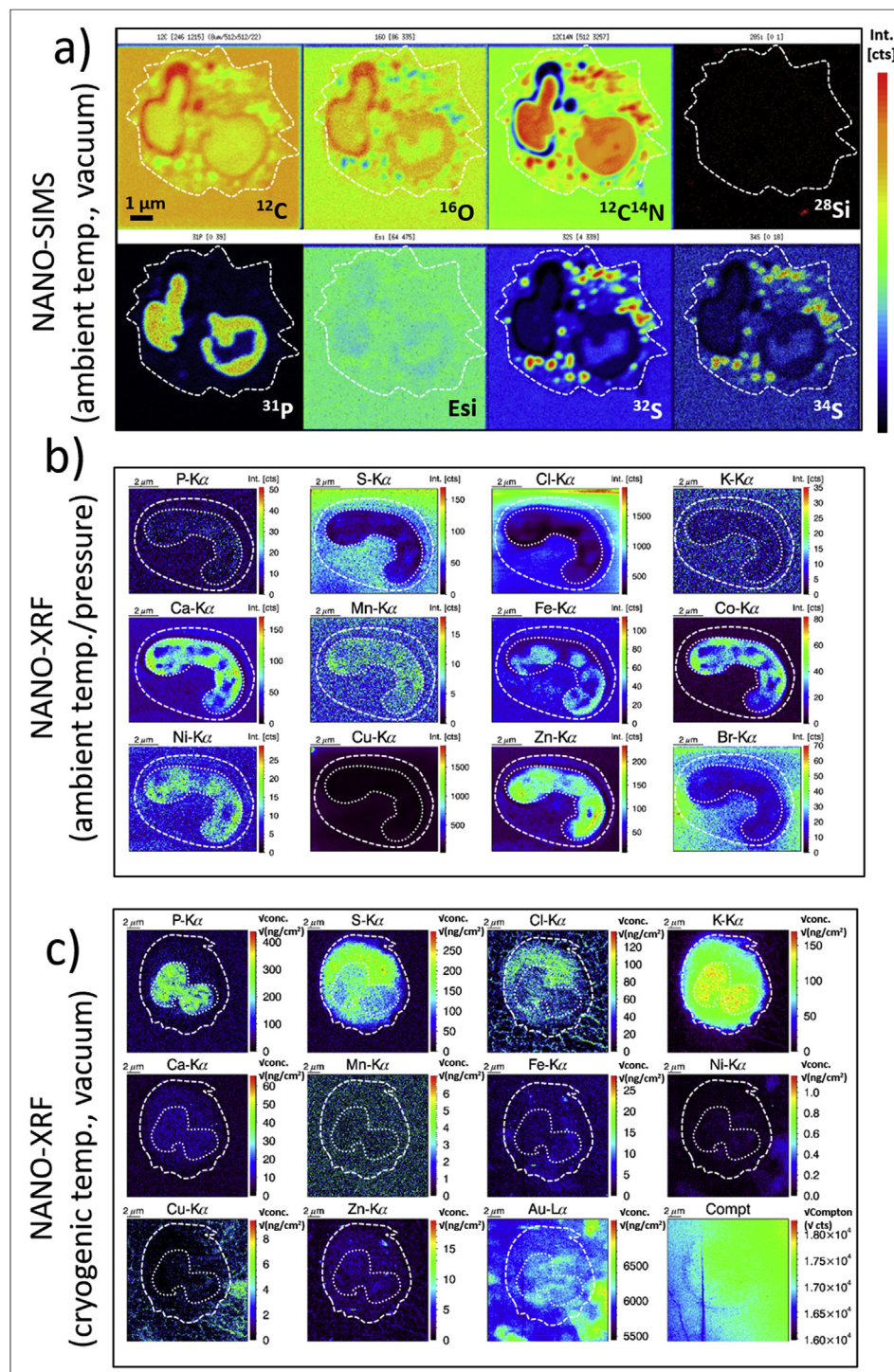
Fig. 3. Comparison of a) nano-SIMS measurements performed under ambient temperature upon high pressure frozen, cryo-substituted PMNs, embedded in Spurr's resin and cut into 500 nm thin section (pixel size 16 nm, approx. 100-200 nm 'true' spatial resolution). Color bar on the right hand side represents secondary ion counts; min. and max. intensity value is provided above each isotope map (between square brackets). b) SR nano-XRF measurements performed under ambient temperature and pressure upon high pressure frozen, cryo-substituted PMNs, embedded in Spurr's resin and cut into 2 μm thin sections (dwell time 300 ms, 50 nm pixel size, expressed in counts) c) SR nano-XRF upon cryofrozen (vitrified) PMNs using automated blotting and plunge freezing (50 ms dwell time, 50 nm pixel size, expressed in ng/cm^2 (square-rooted values concentration values are provided for better contrast of the elements Ca, Fe, Zn). PMN cell and nucleus boundary is indicated with a dashed and dotted line, respectively. (For interpretation of the references to colour in this figure legend, the reader is referred to the Web version of this article.)

removal of chlorine during cryo-substitution. Besides these findings for P, S and Cl, nearly all metals (Ca, Mn, Fe, Co, Ni and Zn) are more pronounced in the PMN nucleus measured with nano-XRF under ambient pressure and temperature (see Fig. 3b), which

may be caused by the higher sensitivity for this set-up or elemental redistribution during sample preparation. An interesting map in Fig. 3c is the map generated by the Au-L fluorescent signal. It does not reflect the presence of gold in the sample, but the presence of

ice crystals/crystallinity in the sample that are diffracting X-ray photons. Then, diffracted photons that are exciting the gold-coated sample holder (used in this set-up) result in gold fluorescence reaching the detector.

2.4. Effect of ice layer thickness on limits of detection (LODs)

To enable XRF analysis of cryofrozen cells, silicon nitride wafers with live, adhered cells are first blotted with filter paper after which ideally, a water layer of few micrometer remains. After plunge freezing, the resulting ice layer still absorbs fluorescence of the lower atomic number elements present in the cell below (e.g., P, S, Cl). Note that a thicker ice layer also results in increased background scatter and increased background fluorescence from the cryogenic sample environment. In order to illustrate the effect of ice layer thickness upon analytical sensitivity, Fig. 4 shows the obtained limits of detections (LODs) in parts-per-million (ppm) and micromolar (μM) for the ID16NI beamline (used for obtaining the results in Fig. 3c). Additionally, the graph shows the LODs which would be obtained when the SRM is covered with 10, 50 and 100 μm of pure ice. From this graph, we clearly see that a covering ice layer of only 10 μm has already a significant effect on the LOD for lower atomic number elements such as P, S and Cl. For larger atomic number elements (starting from manganese here), ice absorption effects are almost negligible. For more information on calculating LODs for different ice layer thickness, we refer to previous work [9]. Increased LODs due to ice can be circumvented by: 1) better control of conditions during cryofixation, 2) preselection of samples with thinnest ice layer (requires specialized equipment such as a cryomicroscope and 3) use of collimators on the detector side, rejecting a larger portion of the background scatter and fluorescence.

3. Materials and Methods

3.1. Cell culture, high pressure freezing and cryosubstitution

In a 45 μL droplet, 2.5×10^4 neutrophils in HEPES-buffered RPMI were seeded onto a 1.4 mm sapphire disk (Leica consumables no. 16706849). To isolate neutrophils from peripheral blood we acquired venous blood from healthy voluntary donors at the Umeå Blodcentralen with informed written consent in accordance to an ethical permission 09–210 M from the regional ethical board in Umeå. All blood samples were taken by trained personnel (not by the authors themselves) and tested negative for HBsAg, HIV 1/2 ab and ag (HIV combo test), anti-HCV and syphilis. The blood samples exclusively served as a source for primary neutrophils. No donor data were used or saved anywhere, nor were any personal data relevant for the study.

NET formation was induced by adding 100 nM PMA or cells were left unstimulated. Stimulated cells were incubated for up to 4 h at 37 °C with 5% CO_2. Then, the medium was carefully removed, cells were washed twice very briefly with a droplet of ultraclean H_2O and 50 μl of 20% w/v BSA in PBS were added onto each sapphire disk as a cryoprotectant. The sapphire disc was then inserted in a membrane carrier (Leica consumables no. 16707898, 1.4 mm diameter, 100 μm thickness) and frozen immediately in a high pressure freezer (EM PACT; Leica Microsystems, Vienna, Austria). Freeze substitution was carried out using a Leica EM AFS2 (Leica Microsystems) in dry acetone with 0.1% glutaraldehyde over 4 days as follows: −90 °C per hour increase for 15 h, and −30 °C for 24 h. Samples were then washed 3 times in pure acetone and slowly warmed up to 4 °C, infiltrated stepwise over 3 days at 4 °C in Spurr's resin (solution composed of 450 g nonenylsuccinic anhydride (NSA), 250 g ERL 4221, 250 g DER 736 and 100 g
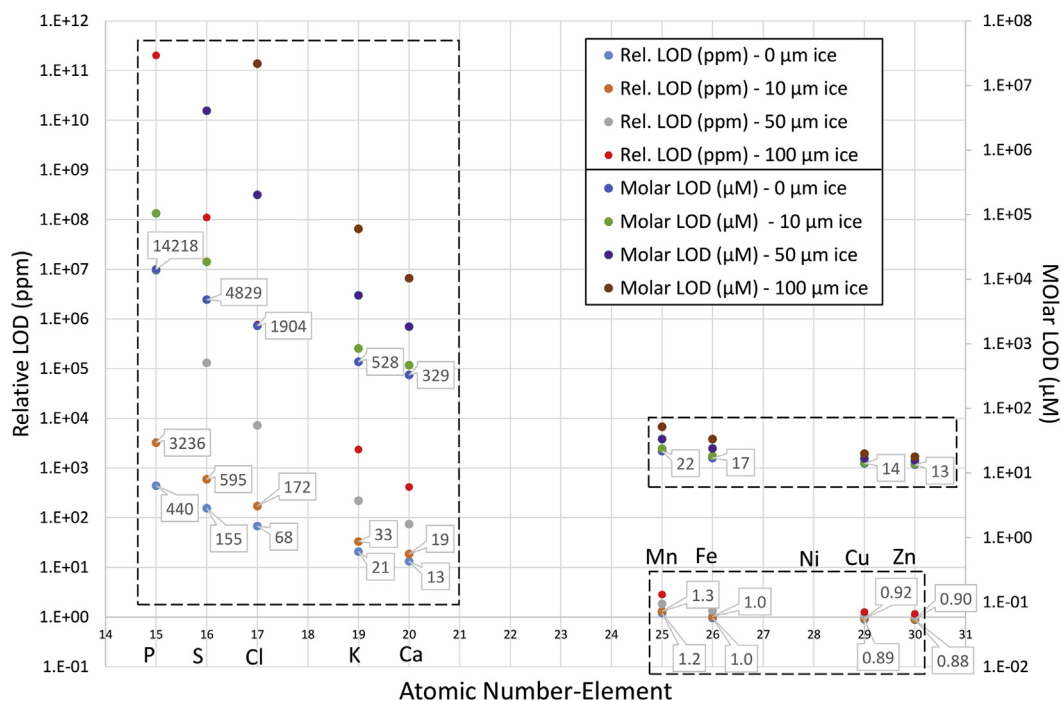

Fig. 4. Relative limit of detection (in ppm, left Y-axis) and molar limit of detection (in μmolar or μM, right Y-axis) obtained from NIST SRM 1577c (bovine liver) at beamline ID16NI. LODs were estimated for the SRM only and for different ice layers of 10-50-100 μm covering the SRM (see legend). LODs were determined for typical scanning conditions at ID16NI: 17 keV excitation energy, high-dose mode (2×10^{11} photons/s), no absorbers in the beam path, 50 ms dwell time and normalized to 200 mA ESRF ring current. (For interpretation of the references to colour in this figure legend, the reader is referred to the Web version of this article.)

dimethylaminoethanol (DMAE) from emsdiasum.com, Hatfield) and embedded in capsules. The polymerization was performed at 70 °C for 16 h.

For TEM analysis of the prepared samples, ultrathin sections (approx. 60 nm) were cut using an ultramicrotome (Leica EM UC6) and post-stained in a Leica EM AC20 for 40 min in uranyl acetate at 20 °C and for 10 min in lead citrate at 20 °C. Grids were viewed with a JEM 1010 transmission electron microscope (JEOL, Tokyo, Japan) operating at 80 kV using Image Plate Technology from Ditabis (Pforzheim, Germany).

For nano-SIMS analysis, thin sections of 500 nm and 1 μm, cut from the Spurr's resin trimmed cube (see above) were deposited on a 5×5 mm^2 silicon chip of 500 μm thickness (4″ diameter, 5×5 mm diced Silicon Wafer, 270 chips/wafer, Ted pella inc., order no. 16008).

For SR nano-XRF analysis under atmospheric conditions, semi-thin sections (2 μm), were cut and deposited on square silicon nitride (Si$_3$N$_4$) ultra-thin membranes in square silicon nitride supporting frames from Silson Ltd, Northampton, UK (3.0×3.0 mm membrane size, 500 nm membrane thickness, 7.5×7.5 mm^2 frame size and 200 μm frame thickness).

3.2. Automated plunge freezing

Silicon nitride membrane frames from Silson Ltd (5×5 mm^2 frame size, 1.5×1.5 mm^2 membrane area, 200 μm frame thickness and 500 nm membrane thickness) were rinsed two times in 70% ethanol and two times in milliQ water before PMNs were cultured as described in previous paragraph 'Cell Culture, High pressure freezing and cryosubstitution'. Then, each wafer was briefly washed via gentle movement through a 0.25 M ammonium formate buffer solution (NH$_4$HCO$_2$, 2.5455 g dissolved in 160 mL milliQ water) for approx. 5 s, which removes the metal-containing medium from the silicon nitride wafers. Both sides of the wafer were then blotted with an automated plunge freezer (Vitrobot™, FEI, The Netherlands) to remove the excess of washing buffer; blotting time was varied between 1 and 2 s. After cryofixation, wafers were put in cryogenic vials with screw caps. Few days before the experiment, samples were shipped to the ESRF using a dry-shipper (Cryoport™, US) with continuous registration and on-line readout of temperature, pressure and slope.

3.3. Nano-SIMS

Nano-SIMS measurements were performed in June 2017 the CAMECA™ NanoSIMS 50 L instrument located at Utrecht University. Silicon chips carrying both 1 μm and 500 nm thin sections were made, but only the 500 nm sections were analyzed with nano-SIMS due to time constraint and better conductivity. Silicon chips were clamped into a nano-SIMS sample holder fabricated for biology purposes using a 5 mm diameter spacer ring. Using the Cs$^+$ source, electron multiplier detectors were adjusted for the following elements: ^{12}C, ^{16}O, ^{12}C^{14}N, ^{28}Si, ^{31}P, ^{32}S and ^{34}S. Secondary electron image (ESI) was acquired as well. Typical current of the primary Cs$^+$ ion beam was 2 pA (picoampere). ^{28}Si served as detection means for the sample support and for optimization purposes. Mass resolving power (MRP) value of up to 11,000 was obtained. All samples were pre-sputtered using the Cs$^+$ source with a higher ion current of 10 pA for approx. 15 min. Note that during the pre-sputtering phase, data acquisition is not possible as this would result in detector overload.

With the aim of detecting metals, the instrument was subsequently tuned with the duoplasmatron O$^-$ source. In this mode, electron multiplier detectors were optimized for the following elements: ^{28}Si, ^{39}K, ^{40}Ca, ^{56}Fe, ^{55}Mn, ^{63}Cu, ^{64}Zn. Other potential

relevant elements detectable with the duoplasmatron oxygen source included Na, Co, Rb and Sr (elements Ni, Se and Co as well, but showed too low signal). Here, a primary ion beam of 100–200 pA was used, compared to the much lower 2 pA for the cesium source. Since the pre-sputtering was harsher for the oxygen source – ultimately reaching the Si wafer – the pre-sputtering step was omitted in order to be sure not having removed the layer of interest. Analysis of all results was done by the Look@SIMS software package [40]. This package autoscales and aligns all plane images using a base mass for alignment before summing all plane intensities.

3.4. SR based nano-XRF analysis under ambient temperature

Non-cryogenic nano-XRF experiment were performed in July 2011 at the former ID22NI beamline located at the European Synchrotron Radiation Facility (ESRF) in Grenoble, France. This instrument was installed at a high-β straight section equipped with two different undulators covering an energy range of 6–70 keV. The ID22NI nanoprobe (currently replaced by the 'Nano-Imaging Nano-Analysis' outstation or NINA, see next paragraph) was dedicated to hard X-ray nano-analysis allowing nano-XRF and absorption/phase contrast nanotomography. X-ray focusing was obtained by a crossed elliptical rhodium (Rh) coated graded-multilayer mirror-pair in the Kirkpatrick-Baez (KB) geometry. X-rays were collected and focused in both vertical and horizontal axis at a glancing angle (<3.5 mrad). The first mirror, coated with a graded multilayer plays both the role of vertical focusing device and monochromator, resulting in a very high flux (10^{12} photons/s) and a medium monochromaticity ($\Delta E/E \approx 10^{-2}$). The beam size was determined by knife-edge scans of a gold (Au) test pattern and determined to be 64 nm vertically and 54 nm horizontally at an excitation energy of 17 keV. For XRF detection, a single Vortex™ silicon drift detector (SDD) with 50 mm^2 active area and lead collimator was used, placed at a 15° angle with respect to the sample surface and at a distance of approx. 20 mm from the sample. Scans were performed in continuous mode with a dwell time of 50 ms/pixel. XRF spectral data was processed using AXIL software (Analysis of X-ray Spectra by Iterative Least Squares) [41] and the in-house developed MICROXRF2 software written in IDL (Interactive Data Language, L3 HarrisGeospatial, Inc.).

3.5. SR nano-XRF experiments under cryogenic conditions

Scanning nano-XRF experiments of cryogenically frozen PMNs were performed at the ESRF's ID16A-NI (Nano-Imaging) beamline in February 2017. ID16-NI provides the world's brightest hard X-ray nanofocus, i.e. 2×10^{11} photons/s, confined within a beam of 27 nm horizontally by 21 nm vertically full-width at half-maximum (FWHM). Beamline techniques include full-field holography, ptychography and X-ray fluorescence. Incident energy upon the X-ray focusing optics housed within the high vacuum sample chamber is 17.1 keV having a spectral bandwidth $\Delta E/E$ of 1%, also 33.6 keV excitation energy can be provided. Measurements are performed in-vacuum and, if desired, under cryogenic conditions. For XRF detection, an array of 6 in-vacuum silicon drift detectors was used (Rayspec Ltd., UK) equipped with beryllium window (no collimator), providing an active area of approx. 300 mm^2, placed at 90° with respect to the incoming beam, but in front of the sample plane by a few mm. Typical measuring time was again 50 ms/pixel. The total sum spectrum of all 6 detectors was used for XRF spectral fitting (see previous paragraph).

Upon the start of the experiment, cryofrozen wafers of interest are transferred into the liquid nitrogen bath of a Leica™ EM VCM (Vacuum Cryo Manipulation System) where they are clamped in a

pre-cooled gold-coated VCT sample holder. The sample holder is then loaded into the Leica™ EM VCT500 (Vacuum Cryo Transfer system). Finally, sample shuttle is attached to the ID16A-NI vacuum chamber and the gold-coated copper cube holding the silicon nitride membrane with deposited PMNs is transferred onto the sample stage of ID16NI beamline. The temperature of the sample holder clamping the sample wafer is continuously monitored and remains constant at approx. $-150\ ^{\circ}C$. For more information on the technical aspects of the beamline, we refer to another manuscript [27].

4. Conclusion & outlook

Synchrotron radiation-based nano-XRF and nano-SIMS are two powerful, label-free methods for elemental imaging at the nanoscale, both recently reaching the 30 nm level. Nano-SIMS has the routine capability of non-metal isotopic imaging (C, N, O, P, S) of main constituents in single cells using a cesium source at the 50 nm level. By the use of a conventional duoplasmatron oxygen source, also metals such as Mn, Fe, Ni, Cu and Zn can be mapped at moderate spatial resolution (200-500 nm). However, samples need to be flat and analyzed in high-vacuum conditions. High pressure freezing (HPF), followed by cryo-substitution and resin embedding is currently the preferred method for routine ultrastructural imaging of cells using TEM, but unfortunately does not necessarily maintain all elemental distributions.

In a first part of our study, we compared SR based nano-XRF (performed under ambient temperature and pressure) and nano-SIMS from the analytical point of view by measuring thin sections of embedded single cells, cut from the same resin cube, but with different slice thickness. Human neutrophils (or PMNs) were used as model cell type and at least five representative cells were analyzed for both techniques. Generally, we found that nano-SIMS is complementary to nano-XRF for chemical imaging as it enables nanoscale (100 nm) mapping of isotopic of elements such as C, O and N, elements which are not accessible with nano-XRF. Nano-XRF, on the other hand, shows its superiority for trace level metal imaging of elements as Ca, Mn, Fe, Ni, Cu and Zn, disregarding the capabilities of a newly developed oxygen RF source. Element distributions obtained by nano-XRF and nano-SIMS (e.g. for phosphorus and sulphur) may differ, not only due to sample preparation artefacts, but also due to inherent differences between both analytical techniques. For example, nano-SIMS probes the upper surface layer of the sample (few nm), whereas nano-XRF has increasing probing depth with increasing atomic number (e.g., few μm for phosphorus, while several mm for zinc). When operated in air, absorption of X-ray fluorescence of lower atomic number elements (e.g., phosphorus, sulphur) may render XRF analysis impossible, favoring (in-vacuum) nano-SIMS analysis.

Little is known on the chemical changes occurring during high pressure freezing, followed by cryo-substitution and embedding of single cells in Spurr's resin. The recent availability of SR nano-XRF analysis in a cryogenic sample environment enables nanochemical imaging of single cells close to their real-life condition. Therefore, in a second part of our study, we compared elemental distributions of PMNs embedded in Spurr's resin with those of entire cryofrozen PMNs, with again a minimum of 5 representative cells. Here, we found large similarities for the element distribution of phosphorous and sulphur for both methods (XRF analysis under cryogenic/non-cryogenic conditions), indicating a (partial) preservation of these elements during the embedding procedure. Likely, sulphur and phosphorous are more chemically bound to the cell structure, making them less susceptible to migration during the substitution process. Potassium and chlorine were more pronounced in cryofrozen PMNs compared to PMNs embedded in Spurr's resin, indicating significant removal of these elements after cryo-substitution. On the other hand, thin sections of PMNs measured with SR nano-XRF under ambient temperature showed higher relative intensity of (trace level) metals like Ca, Mn, Fe, Ni and Zn in the nucleus, which could be due to a sample preparation artefact or due to the higher sensitivity of nano-XRF effected under non-cryogenic conditions, suffering less from X-ray scatter and increased background.

Recently, an oxygen plasma sources based on a radiofrequency (RF) field has been developed, reaching 40 nm resolution and 5-45 times higher sensitivity for electropositive elements, creating new possibilities for trace level metal imaging using nano-SIMS. Further experiments are required to explore the potential of this new source for imaging trace metals like Mn, Fe, Cu and Zn in single cells. The necessity of nano-SIMS to measure cells in a high vacuum environment, requiring sample embedding, remains a weakness of the technique. The gold standard for nanochemical imaging of trace metals in single cells close to the native state currently remains SR nano-XRF equipped with a cryogenic sample environment. Note however that the cryofixation procedure itself can still lead to morphological artefacts. It is expected that, in the next decade, nano-SIMS will soon follow in the transition from the analysis of embedded cells towards analysis of cell cryosections. Issues such as cryogenic sample transfer and an ice layer covering the sample will also need to be addressed here. In general, we can state that SR nano-XRF and nano-SIMS stand side-by-side in elemental analysis as two supplementary analytical techniques, each with their own pros and cons. Where SR nano-XRF has the advantage of in-depth analysis, (ultra)trace level metal sensitivity, sample-independent nanoscopic resolution and ability to measure cryofrozen samples, nano-SIMS has the advantage of mapping isotopes, detecting light elements and fast repetitive mapping.

Data availability statement

The ESRF Council has recently endorsed the implementation of a Data Policy for data taken at the ESRF beamlines. The Data Policy is based on the PaNdata Data Policy which was a deliverable of the European FP7 project PaN-data Europe (http://pan-data.eu/) delivered in 2011. The Data Policy defines the ESRF as the custodian of raw data and metadata. The metadata is stored in the ICAT metadata catalogue (https://icatproject.org/) which can be accessed online (https://icat.esrf.fr) to browse and download (meta)data. The metadata will be stored in the ICAT metadata catalogue which can be accessed online to browse and download (meta)data. A three-year embargo period applies after each ESRF measurement during which the experimental team has the right to have sole access to the data, renewable if necessary. The (meta)data related to the experiment of this manuscript (LS-2550) performed in February 2017 will therefore be released entirely in February 2020 under a CC-BY-4 license with open access to anyone who has registered with the ESRF data portal.

Declaration of competing interest

The author(s) declare no conflict of interest.

CRediT authorship contribution statement

Björn De Samber: Conceptualization, Data curation, Investigation, Software, Visualization, Writing - original draft. **Riet De Rycke:** Methodology, Investigation, Visualization. **Michiel De Bruyne:** Methodology. **Michiel Kienhuis:** Visualization, Methodology. **Linda Sandblad:** Resources, Methodology. **Sylvain Bohic:** Methodology, Conceptualization. **Peter Cloetens:** Resources,

Investigation, Funding acquisition. **Constantin Urban:** Investigation, Resources, Supervision. **Lubos Polerecky:** Investigation, Methodology, Resources, Writing - original draft, Funding acquisition, Writing - review & editing. **Laszlo Vincze:** Methodology, Resources, Supervision, Funding acquisition.

Acknowledgements

References

[1] P.L. Clode, R.A. Stern, A.T. Marshall, Subcellular imaging of isotopically labeled carbon compounds in a biological sample by ion microprobe (NanoSIMS), Microsc. Res. Tech. 70 (2007) 220–229.

[2] A. Delaune, A. Cabin-Flaman, G. Legent, D. Gibouin, C. Smet-Nocca, F. Lefebvre, A. Benecke, M. Vasse, C. Ripoll, 50nm-Scale localization of single unmodified, isotopically enriched, proteins in cells, PloS One 8 (2013) 12.

[3] C. Guillermier, M.L. Steinhauser, C.P. Lechene, Quasi-simultaneous acquisition of nine secondary ions with seven detectors on NanoSIMS50L: application to biological samples, Surf. Interface Anal. 46 (2014) 150–153.

[4] C. Lechene, F. Hillion, G. McMahon, D. Benson, A.M. Kleinfeld, J.P. Kampf, D. Distel, Y. Luyten, J. Bonventre, D. Hentschel, K.M. Park, S. Ito, M. Schwartz, G. Benichou, G. Slodzian, High-resolution quantitative imaging of mammalian and bacterial cells using stable isotope mass spectrometry, J. Biol. 5 (2006) 20.

[5] R.F.S. Lee, T. Riedel, S. Escrig, C. Maclachlan, G.W. Knott, C.A. Davey, K. Johnsson, A. Meibom, P.J. Dyson, Differences in cisplatin distribution in sensitive and resistant ovarian cancer cells: a TEM/NanoSIMS study, Metallomics 9 (2017) 1413–1420.

[6] C. Quintana, T.D. Wu, B. Delatour, M. Dhenain, J.L. Guerquin-Kern, A. Croisy, Morphological and chemical studies of pathological human and mice brain at the subcellular level: correlation between light, electron, and NanoSIMS microscopies, Microsc. Res. Tech. 70 (2007) 281–295.

[7] A. Carmona, P. Cloetens, G. Deves, S. Bohic, R. Ortega, Nano-imaging of trace metals by synchrotron X-ray fluorescence into dopaminergic single cells and neurite-like processes, J. Anal. At. Spectrom. 23 (2008) 1083–1088.

[8] S. Corezzi, L. Urbanelli, P. Cloetens, C. Emiliani, L. Helfen, S. Bohic, F. Elisei, D. Fioretto, Synchrotron-based X-ray fluorescence imaging of human cells labeled with CdSe quantum dots, Anal. Biochem. 388 (2009) 33–39.

[9] B. De Samber, E. Meul, B. Laforce, B. De Paepe, J. Smet, M. De Bruyne, R. De Rycke, S. Bohic, P. Cloetens, R. Van Coster, P. Vandenabeele, T. Vanden Berghe, Nanoscopic X-ray fluorescence imaging and quantification of intracellular key-elements in cryofrozen Friedreich's ataxia fibroblasts, PloS One 13 (2018) 24.

[10] R. Ortega, P. Cloetens, G. Deves, A. Carmona, S. Bohic, Iron storage within dopamine neurovesicles revealed by chemical nano-imaging, PloS One 2 (2007) 6.

[11] C. Sanchez-Cano, I. Romero-Canelon, Y. Yang, I.J. Hands-Portman, S. Bohic, P. Cloetens, P.J. Sadler, Synchrotron X-ray fluorescence nanoprobe reveals target sites for organo-osmium complex in human ovarian cancer cells, Chem. Eur J. 23 (2017) 2512–2516.

[12] B. De Samber, K.A.C. De Schamphelaere, C.R. Janssen, B. Vekemans, R. De Rycke, G. Martinez-Criado, R. Tucoulou, P. Cloetens, L. Vincze, Hard X-ray nanoprobe investigations of the subtissue metal distributions within Daphnia magna, Anal. Bioanal. Chem. 405 (2013) 6061–6068.

[13] B. De Samber, M.J. Niemiec, B. Laforce, J. Garrevoet, E. Vergucht, R. De Rycke, P. Cloetens, C.F. Urban, L. Vincze, Probing intracellular element concentration changes during neutrophil extracellular trap formation using synchrotron radiation based X-ray fluorescence, PloS One 11 (2016).

[14] J.F. Collingwood, F. Adams, Chemical imaging analysis of the brain with X-ray methods, Spectroc. Acta Pt. B-Atom. Spectr. 130 (2017) 101–118.

[15] D. Studer, M. Michel, M. Muller, HIGH-PRESSURE freezing comes OF age, Scanning Microsc. (1989) 253–269.

[16] D. Studer, W. Graber, A. Al-Amoudi, P. Eggli, A new approach for cryofixation by high-pressure freezing, J. Microsc. 203 (2001) 285–294.

[17] G.F. Zhang, L.A. Staehelin, Functional compartmentation OF the golgi-apparatus OF plant-cells - immunocytochemical analysis OF high-pressure frozen-substituted and freeze-substituted sycamore maple suspension-culture cells, Plant Physiol. 99 (1992) 1070–1083.

[18] L.A. Staehelin, T.H. Giddings, J.Z. Kiss, F.D. Sack, Macromolecular differentiation OF golgi stacks IN root-tips OF arabidopsis and nicotiana seedlings as visualized IN high-pressure frozen and freeze-substituted samples, Protoplasma 157 (1990) 75–91.

[19] S. Chen, J. Deng, Y. Yuan, C. Flachenecker, R. Mak, B. Hornberger, Q. Jin, D. Shu, B. Lai, J. Maser, C. Roehrig, T. Paunesku, S.C. Gleber, D.J. Vine, L. Finney, J. VonOsinski, M. Bolbat, I. Spink, Z. Chen, J. Steele, D. Trapp, J. Irwin, M. Feser, E. Snyder, K. Brister, C. Jacobsen, G. Woloschak, S. Vogt, The Bionanoprobe: hard X-ray fluorescence nanoprobe with cryogenic capabilities, J. Synchrotron Radiat. 21 (2014) 66–75.

[20] N. Borregaard, Neutrophils, from marrow to microbes, Immunity 33 (2010) 657–670.

[21] W.M. Nauseef, N. Borregaard, Neutrophils at work, Nat. Immunol. 15 (2014) 602–611.

[22] V. Brinkmann, U. Reichard, C. Goosmann, B. Fauler, Y. Uhlemann, D.S. Weiss, Y. Weinrauch, A. Zychlinsky, Neutrophil extracellular traps kill bacteria, Science 303 (2004) 1532–1535.

[23] V. Brinkmann, A. Zychlinsky, Beneficial suicide: why neutrophils die to make NETs, Nat. Rev. Microbiol. 5 (2007) 577–582.

[24] Q. Remijsen, T.W. Kuijpers, E. Wirawan, S. Lippens, P. Vandenabeele, T. Vanden Berghe, Dying for a cause: NETosis, mechanisms behind an antimicrobial cell death modality, Cell Death Differ. 18 (2011) 581–588.

[25] C.F. Urban, D. Ermert, M. Schmid, U. Abu-Abed, C. Goosmann, W. Nacken, V. Brinkmann, P.R. Jungblut, A. Zychlinsky, Neutrophil extracellular traps contain calprotectin, a cytosolic protein complex involved in host defense against Candida albicans, PLoS Pathog. 5 (2009) 18.

[26] M.J. Niemiec, B. De Samber, J. Garrevoet, E. Vergucht, B. Vekemans, R. De Rycke, E. Bjorn, L. Sandblad, G. Wellenreuther, G. Falkenberg, P. Cloetens, L. Vincze, C.F. Urban, Trace element landscape of resting and activated human neutrophils on the sub-micrometer level, Metallomics 7 (2015) 996–1010.

[27] J.C. Da Silva, A. Pacureanu, Y. Yang, S. Bohic, C. Morawe, R. Barrett, P. Cloetens, Efficient concentration of high-energy x-rays for diffraction-limited imaging resolution, Optica 4 (2017) 492–495.

[28] C.P. Lechene, R.R. Warner, Microbeam Analysis in Biology, Academic Press, Inc. (LONDON) LTD, 1979.

[29] d.R.D. Rycke, Personal Communication.

[30] F.C. Fang, Antimicrobial reactive oxygen and nitrogen species: concepts and controversies, Nat. Rev. Microbiol. 2 (2004) 820–832.

[31] T. Nakatsuji, R.L. Gallo, Antimicrobial peptides: old molecules with new ideas, J. Invest. Dermatol. 132 (2012) 887–895.

[32] J. Malherbe, F. Penen, M.P. Isaure, J. Frank, G. Hause, D. Dobritzsch, E. Gontier, F. Horreard, F. Hillion, D. Schaumloffel, A new radio frequency plasma oxygen primary ion source on nano secondary ion mass spectrometry for improved lateral resolution and detection of electropositive elements at single cell level, Anal. Chem. 88 (2016) 7130–7136.

[33] I. Striz, I. Trebichavsky, Calprotectin - a pleiotropic molecule in acute and chronic inflammation, Physiol. Res. 53 (2004) 245–253.

[34] T.E. Kehl-Fie, S. Chitayat, M.I. Hood, S. Damo, N. Restrepo, C. Garcia, K.A. Munro, W.J. Chazin, E.P. Skaar, Nutrient metal sequestration by calprotectin inhibits bacterial superoxide defense, enhancing neutrophil killing of Staphylococcus aureus, Cell Host Microbe 10 (2011) 158–164.

[35] T.G. Nakashige, B. Zhang, C. Krebs, E.M. Nolan, Human calprotectin is an iron-sequestering host-defense protein, Nat. Chem. Biol. 11 (2015) 765–771.

[36] S.J. Dixon, B.R. Stockwell, The role of iron and reactive oxygen species in cell death, Nat. Chem. Biol. 10 (2014) 9–17.

[37] B. De Samber, M.J. Niemiec, B. Laforce, J. Garrevoet, E. Vergucht, R. De Rycke, P. Cloetens, C.F. Urban, L. Vincze, Probing intracellular element concentration changes during neutrophil extracellular trap formation using synchrotron radiation based X-ray fluorescence, PloS One 11 (2016), e0165604.

[38] G. Martinez-Criado, R. Tucoulou, P. Cloetens, P. Bleuet, S. Bohic, J. Cauzid, I. Kieffer, E. Kosior, S. Laboure, S. Petitgirard, A. Rack, J.A. Sans, J. Segura-Ruiz, H. Suhonen, J. Susini, J. Villanova, Status of the hard X-ray microprobe beamline ID22 of the European synchrotron radiation facility, J. Synchrotron Radiat. 19 (2012) 10–18.

[39] J. Pierson, J.J. Fernandez, E. Bos, S. Amini, H. Gnaegi, M. Vos, B. Bel, F. Adolfsen, J.L. Carrascosa, P.J. Peters, Improving the technique of vitreous cryo-sectioning for cryo-electron tomography: electrostatic charging for section attachment and implementation of an anti-contamination glove box, J. Struct. Biol. 169 (2010) 219–225.

[40] L. Polerecky, B. Adam, J. Milucka, N. Musat, T. Vagner, M.M.M. Kuypers, Look@ NanoSIMS - a tool for the analysis of nanoSIMS data in environmental microbiology, Environ. Microbiol. 14 (2012) 1009–1023.

[41] B. Vekemans, K. Janssens, L. Vincze, F. Adams, P. Vanespen, Analysis OF X-RAY-SPECTRA BY iterative least-squares (AXIL) - new developments, X Ray Spectrom. 23 (1994) 278–285.